12-16-2013

Direct Coupling of Photonic Modes and Surface Plasmon Polaritons Observed in 2-photon PEEM

Robert Campbell Word
Portland State University

Joseph Fitzgerald
Portland State University

Rolf Könenkamp
Portland State University, rkoe@pdx.edu

Citation Details

Word, Robert C., Joseph PS Fitzgerald, and Rolf Könenkamp. "Direct coupling of photonic modes and surface plasmon polaritons observed in 2-photon PEEM." Optics Express 21.25 (2013): 30507-30520.

Direct coupling of photonic modes and surface plasmon polaritons observed in 2-photon PEEM

Robert C. Word,[*] Joseph P. S. Fitzgerald, and Rolf Könenkamp

Department of Physics, Portland State University, Portland, Oregon, 97207, USA
[*]*wordr@pdx.edu*

Abstract: We report the direct microscopic observation of optical energy transfer from guided photonic modes in an indium tin oxide (ITO) thin film to surface plasmon polaritons (SPP) at the surfaces of a single crystalline gold platelet. The photonic and SPP modes appear as an interference pattern in the photoelectron emission yield across the surface of the specimen. We explore the momentum match between the photonic and SPP modes in terms of simple waveguide theory and the three-layer slab model for bound SPP modes of thin metal films. We show that because the gold is thin (30-40 nm), two SPP modes exist and that momentum of the spatially confined asymmetric field mode coincides with the dominant mode of the ITO waveguide. The results demonstrate that photoemission electron microscopy (PEEM) can be an important tool for the observation of photonic to SPP interactions in the study of integrated photonic circuits.

OCIS codes: (240.6680) Surface plasmons; (240.6675) Surface photoemission and photoelectron spectroscopy; (240.0240) Optics at surfaces; (130.0130) Integrated optics.

References and links

1. H. Jans and Q. Huo, "Gold nanoparticle-enabled biological and chemical detection and analysis," Chem. Soc. Rev. **41**(7), 2849–2866 (2012).
2. D. K. Gramotnev and S. I. Bozhevolnyi, "Plasmonics beyond the diffraction limit," Nat. Photonics **4**(2), 83–91 (2010).
3. J. Zhang, L. Zhang, and W. Xu, "Surface plasmon polaritons: physics and applications," J. Phys. D Appl. Phys. **45**(11), 113001 (2012).
4. T. Feichtner, O. Selig, M. Kiunke, and B. Hecht, "Evolutionary optimization of optical antennas," Phys. Rev. Lett. **109**(12), 127701 (2012).
5. B. Lee, I.-M. Lee, S. Kim, D.-H. Oh, and L. Hesselink, "Review on subwavelength confinement of light with plasmonics," J. Mod. Opt. **57**(16), 1479–1497 (2010).
6. C. Y. Jun and I. Brener, "Optical manipulation with plasmonic beam shaping antenna structures," Adv. Optoelectron. **2012**, 595646 (2012).
7. G. V. Naik, V. M. Shalaev, and A. Boltasseva, "Alternative plasmonic materials: beyond gold and silver," Adv. Mater. **25**(24), 3264–3294 (2013).
8. J. B. Khurgin and A. Boltasseva, "Reflecting upon the losses in plasmonics and metamaterials," MRS Bull. **37**(08), 768–779 (2012).
9. X. Guo, M. Qiu, J. Bao, B. J. Wiley, Q. Yang, X. Zhang, Y. Ma, H. Yu, and L. Tong, "Direct coupling of plasmonic and photonic nanowires for hybrid nanophotonic components and circuits," Nano Lett. **9**(12), 4515–4519 (2009).
10. J. R. Krenn and J.-C. Weeber, "Surface plasmon polaritons in metal stripes and wires," Philos. Trans. R. Soc. London, Ser. A **362**, 739–756 (2004).
11. P. Dvořák, T. Neuman, L. Břínek, T. Šamořil, R. Kalousek, P. Dub, P. Varga, and T. Šikola, "Control and near-field detection of surface plasmon interference patterns," Nano Lett. **13**(6), 2558–2563 (2013).
12. M. Bosman, E. Ye, S.F. Tan, C.A. Nijhuis, J.K.W. Yang, R. Marty, A. Mlayah, A. Arbouet, C. Girard, and M.-Y. Han, "Surface plasmon damping quantified with an electron nanoprobe," Sci. Rep. **3**, 1312 (2012).
13. T. Coenen, E. J. R. Vesseur, and A. Polman, "Deep subwavelength spatial characterization of angular emission from single-crystal Au plasmonic ridge nanoantennas," ACS Nano **6**(2), 1742–1750 (2012).
14. R. Vogelgesang and A. Dmitriev, "Real-space imaging of nanoplasmonic resonances," Analyst (Lond.) **135**(6), 1175–1181 (2010).
15. L. Douillard and F. Charra, "Photoemission electron microscopy, a tool for plasmonics," J. Electron Spectrosc. Relat. Phenom. **189**(Supplement), 24–29 (2013).

#200567 - $15.00 USD Received 4 Nov 2013; revised 26 Nov 2013; accepted 27 Nov 2013; published 4 Dec 2013

16. A. Grubisic, E. Ringe, C. M. Cobley, Y. Xia, L. D. Marks, R. P. Van Duyne, and D. J. Nesbitt, “Plasmonic near-electric field enhancement effects in ultrafast photoelectron emission: correlated spatial and laser polarization microscopy studies of individual Ag nanocubes,” Nano Lett. **12**(9), 4823–4829 (2012).
17. J. P. S. Fitzgerald, R. C. Word, S. D. Saliba, and R. Könenkamp, “Photonic near-field imaging in multiphoton photoemission electron microscopy,” Phys. Rev. B **87**(20), 205419 (2013).
18. C. Lemke, T. Leißner, S. Jauernik, A. Klick, J. Fiutowski, J. Kjelstrup-Hansen, H.-G. Rubahn, and M. Bauer, “Mapping surface plasmon polariton propagation via counter-propagating light pulses,” Opt. Express **20**(12), 12877–12884 (2012).
19. N. M. Buckanie, P. Kirschbaum, S. Sindermann, and F.-J. Heringdorf, “Interaction of light and surface plasmon polaritons in Ag islands studied by nonlinear photoemission microscopy,” Ultramicroscopy **130**, 49–53 (2013).
20. D. Bayer, C. Wiemann, O. Gaier, M. Bauer, and M. Aeschlimann, “Time-resolved 2PPE and time-resolved PEEM as a probe of LSP’s in silver nanoparticles,” J. Nanomater. **2008**, 249514 (2008).
21. C. Awada, T. Popescu, L. Douillard, F. Charra, A. Perron, H. Yockell-Lelièvre, A.-L. Baudrion, P.-M. Adam, and R. Bachelot, “Selective excitation of plasmon resonances of single Au triangles by polarization-dependent light excitation,” J. Phys. Chem. C **116**(27), 14591–14598 (2012).
22. R. C. Word, T. Dornan, and R. Könenkamp, “Photoemission from localized surface plasmons in fractal metal nanostructures,” Appl. Phys. Lett. **96**(25), 251110 (2010).
23. A. Kubo, Y. S. Jung, H. K. Kim, and H. Petek, “Femtosecond microscopy of localized and propagating surface plasmons in silver gratings,” J. Phys. B **40**(11), S259–S272 (2007).
24. R. C. Word, J. P. S. Fitzgerald, and R. Konenkamp, “Direct imaging of optical diffraction in photoemission electron microscopy,” Appl. Phys. Lett. **103**(2), 021118 (2013).
25. E. Flück, M. Hammer, A. M. Otter, J. P. Korterik, L. Kuipers, and N. F. van Hulst, “Amplitude and phase evolution of optical fields inside periodic photonic structures,” J. Lightwave Technol. **21**(5), 1384–1393 (2003).
26. L. Stern, B. Desiatov, I. Goykhman, G. M. Lerman, and U. Levy, “Near field phase mapping exploiting intrinsic oscillations of aperture NSOM probe,” Opt. Express **19**(13), 12014–12020 (2011).
27. J.-S. Huang, V. Callegari, P. Geisler, C. Brüning, J. Kern, J. C. Prangsma, X. Wu, T. Feichtner, J. Ziegler, P. Weinmann, M. Kamp, A. Forchel, P. Biagioni, U. Sennhauser, and B. Hecht, “Atomically flat single-crystalline gold nanostructures for plasmonic nanocircuitry,” Nat. Commun. **1**(9), 150 (2010).
28. R. Könenkamp, R. C. Word, J. Fitzgerald, A. Nadarajah, and S. Saliba, “Controlled spatial switching and routing of surface plasmons in designed single-crystalline gold nanostructures,” Appl. Phys. Lett. **101**(14), 141114 (2012).
29. S. Kumar, Y.-W. Lu, A. Huck, and U. L. Andersen, “Propagation of plasmons in designed single crystalline silver nanostructures,” Opt. Express **20**(22), 24614–24622 (2012).
30. B. J. Wiley, D. J. Lipomi, J. Bao, F. Capasso, and G. M. Whitesides, “Fabrication of surface plasmon resonators by nanoskiving single-crystalline gold microplates,” Nano Lett. **8**(9), 3023–3028 (2008).
31. J.-P. Tetienne, A. Bousseksou, D. Costantini, Y. De Wilde, and R. Colombelli, “Design of an integrated coupler for the electrical generation of surface plasmon polaritons,” Opt. Express **19**(19), 18155–18163 (2011).
32. S.-Y. Park, J. T. Kim, J.-S. Shin, and S.-Y. Shin, “Hybrid vertical directional coupling between a long range surface plasmon polariton waveguide and a dielectric waveguide,” Opt. Commun. **282**(23), 4513–4517 (2009).
33. H. Ditlbacher, N. Galler, D. M. Koller, A. Hohenau, A. Leitner, F. R. Aussenegg, and J. R. Krenn, “Coupling dielectric waveguide modes to surface plasmon polaritons,” Opt. Express **16**(14), 10455–10464 (2008).
34. A. Abbas, M. J. Linman, and Q. Cheng, “New trends in instrumental design for surface plasmon resonance-based biosensors,” Biosens. Bioelectron. **26**(5), 1815–1824 (2011).
35. S. R. Seshadri, “Attenuated total reflection method of excitation of the surface polariton in the Kretschmann configuration,” J. Appl. Phys. **70**(7), 3647–3654 (1991).
36. W. Johnstone, G. Stewart, T. Hart, and B. Culshaw, “Surface plasmon polaritons in thin metal films and their role in fiber optic polarizing devices,” J. Lightwave Technol. **8**(4), 538–544 (1990).
37. P. Berini, “Long-range surface plasmon polaritons,” Adv. Opt. Photon. **1**(3), 484–588 (2009).
38. J. J. Burke, G. I. Stegeman, and T. Tamir, “Surface-polariton-like waves guided by thin, lossy metal films,” Phys. Rev. B Condens. Matter **33**(8), 5186–5201 (1986).
39. L. Wendler and R. Haupt, “Long-range surface plasmon-polaritons in asymmetric layer structures,” J. Appl. Phys. **59**(9), 3289 (1986).
40. F. Yang, J. R. Sambles, and G. W. Bradberry, “Long-range surface modes supported by thin films,” Phys. Rev. B Condens. Matter **44**(11), 5855–5872 (1991).
41. Z. Guo, Y. Zhang, Y. DuanMu, L. Xu, S. Xie, and N. Gu, “Facile synthesis of micrometer-sized gold nanoplates through an aniline-assisted route in ethylene glycol solution,” Colloids Surf. **278**(1-3), 33–38 (2006).
42. R. Könenkamp, R. C. Word, G. F. Rempfer, T. Dixon, L. Almaraz, and T. Jones, “5.4 nm spatial resolution in biological photoemission electron microscopy,” Ultramicroscopy **110**(7), 899–902 (2010).
43. G. F. Rempfer, D. M. Deslodge, W. P. Skoczylas, and O. H. Griffith, “Simultaneous correction of spherical and chromatic aberrations with an electron mirror: an electron optical achromat,” Microsc. Microanal. **3**, 14–27 (1997).
44. M. Merschdorf, W. Pfeiffer, A. Thon, S. Voll, and G. Gerber, “Photoemission from multiply excited surface plasmons in Ag nanoparticles,” Appl. Phys., A Mater. Sci. Process. **71**(5), 547–552 (2000).
45. R. G. Hunsperger, *Integrated Optics: Theory and Technology* (Springer, 2009).
46. W. Rechberger, A. Hohenau, A. Leitner, J. Krenn, B. Lamprecht, and F. Aussenegg, “Optical properties of two

interacting gold nanoparticles," Opt. Commun. **220**(1-3), 137–141 (2003).
47. P. Albella, B. Garcia-Cueto, F. González, F. Moreno, P. C. Wu, T.-H. Kim, A. Brown, Y. Yang, H. O. Everitt, and G. Videen, "Shape matters: plasmonic nanoparticle shape enhances interaction with dielectric substrate," Nano Lett. **11**(9), 3531–3537 (2011).
48. M. W. Knight, Y. Wu, J. B. Lassiter, P. Nordlander, and N. J. Halas, "Substrates matter: influence of an adjacent dielectric on an individual plasmonic nanoparticle," Nano Lett. **9**(5), 2188–2192 (2009).
49. D. Rosenblatt, A. Sharon, and A. A. Friesem, "Resonant grating waveguide structures," Quantum Electron. **33**, 2038–2059 (1997).
50. S. A. Maier, *Plasmonics: Fundamentals and Applications* (Springer, 2007).
51. P. Berini, "Plasmon-polariton waves guided by thin lossy metal films of finite width: Bound modes of asymmetric structures," Phys. Rev. B **63**(12), 125417 (2001).
52. G. V. Naik, J. Kim, and A. Boltasseva, "Oxides and nitrides as alternative plasmonic materials in the optical range [Invited]," Opt. Mater. Express **1**(6), 1090–1099 (2011).
53. Sopra Group, *N & K database*. Bois Colombes, France.
54. P. B. Johnson and R. W. Christy, "Optical constants of the noble metals," Phys. Rev. B **6**(12), 4370–4379 (1972).
55. W.-J. Lee, J.-E. Kim, H. Y. Park, and M.-H. Lee, "Silver superlens using antisymmetric surface plasmon modes," Opt. Express **18**(6), 5459–5465 (2010).
56. R. Slavík, J. Homola, and H. Vaisocherová, "Advanced biosensing using simultaneous excitation of short and long range surface plasmons," Meas. Sci. Technol. **17**(4), 932–938 (2006).
57. P. Berini and I. De Leon, "surface plasmon–polariton amplifiers and lasers," Nat. Photonics **4**, 382–387 (2011).
58. C. Lemke, C. Schneider, T. Leißner, D. Bayer, J. W. Radke, A. Fischer, P. Melchior, A. B. Evlyukhin, B. N. Chichkov, C. Reinhardt, M. Bauer, and M. Aeschlimann, "Spatiotemporal characterization of SPP pulse propagation in two-dimensional plasmonic focusing devices," Nano Lett. **13**(3), 1053–1058 (2013).

1. Introduction

Practical application of surface plasmon resonance (SPR) is now well-established in the field of molecular sensing with particular success in biosensing [1]. In this arena SPR-tunable metal structures (typically gold) are used to detect minute changes in the dielectric environment. Applications in other fields are subjects of great interest. For instance, propagating surface plasmon waves or surface plasmon polaritons (SPPs) can be employed in nanophotonic circuits [2]. In comparison to molecular sensing, most research on propagating surface plasmons is still at a fundamental level [3]. Questions remain as to the most effective shapes for plasmonic antennas [4,5] and conduits [6], better materials for their fabrication [7,8], and of the best methods for interfacing photonic and plasmonic components [9]. A key to the success of this research is the continuing development of instrumentation and methods for visualizing SPPs.

Near-field distributions of light and SPPs are typically observed by scanning methods such as photon scanning tunneling microscopy (PSTM) [10], near-field scanning optical microscopy (NSOM) [11], electron energy-loss spectroscopy (EELS) [12], and cathodoluminescence [13]. Photoelectron emission microscopy (PEEM) is a probe-free non-scanning technique in which the surface of the specimen is illuminated by light, which emits electrons from the specimen via the photoelectric effect [14,15]. The electrons are accelerated into an electron optical system and ultimately recorded by a CCD camera. As an electron microscope, the resolution of PEEM is limited by electron optics.

Photoelectron yield depends on the target material's work function, geometry and structure, and the strength of the local electric field, which is influenced by topography and the superposition of various optical phenomena, including SPPs. Conventional PEEM operates in the ultraviolet and x-ray spectral range, whereas SPPs are typically more interesting at longer wavelengths. The bridge between PEEM and the study of SPPs was the development of inexpensive ultrafast lasers, which make multi-photon or *n*P-PEEM viable up to the near IR. Furthermore, the nonlinearity of *n*P-PEEM is particularly useful for the study of SPPs, bound photonic waves, and other types of strong optical fields [16,17]. Over the years, investigators have demonstrated PEEM's ability to image propagating SPPs on metal films [18,19] and localized SPPs on nanoparticles [20], gold triangle antennas [21], fractal holey films [22], and gratings [23]. In a recent report we demonstrated that PEEM may be used to visualize the bound photonic fields in a thin film waveguide [17], and the surface near-fields in vacuum [24]. The results are qualitatively similar to those obtained by PSTM [25] and NSOM [26].

Here we report the use of 2P-PEEM to observe energy transfer of light guided by indium tin oxide (ITO) thin film to a SPP on a very thin gold platelet. Nanocrystalline gold and silver platelets have been suggested as raw materials for the construction of tailor-made plasmonic antennae. The platelets can be shaped by, for example, focused ion beam (FIB) milling [27–29] or nanoskiving [30]. Devices based on the concept of a dielectric waveguide coupled to a metal film SPP waveguide have been proposed as possible photonic circuit elements [31–33]. In this respect, our configuration can be thought of as a simple photonic interconnect. At the wavelength of light used in this study (λ_0 = 410 nm), dissipative losses in gold are quite high and applications involving SPPs will be necessarily short-ranged. Nonetheless, concepts and insights discussed here can be applied to cases where longer wavelengths of light permit longer range SPPs.

In this study we carefully searched for single-crystalline gold platelets with suitable thinness for which we could construct a waveguide and test for photonic to SPP wave coupling. For this the ITO's thickness must be carefully considered since it determines the properties of the modes carried in the ITO. A SPP mode on the gold platelet must match one of the modes of the underlying waveguide for coupling to take place. We will discuss the calculation of waveguide and SPP modes and their matching conditions in depth in this paper.

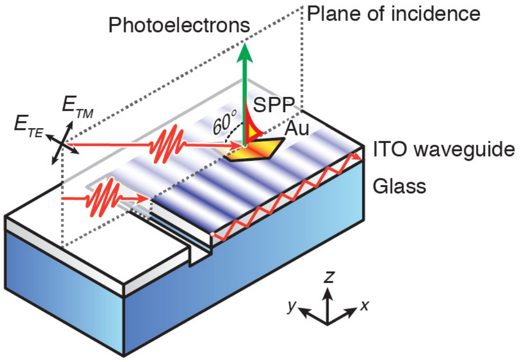

Fig. 1. In the experiment an ultrafast laser beam is coupled into an indium tin oxide (ITO) waveguide via diffraction at a slit. The guided photonic wave travels underneath a gold platelet where it is channeled into a surface plasmon polariton (SPP). The progress of the photonic mode and SPP is observed as interference-based modulation to the photoemission yield. Polarization direction (TE or TM) of the incident electric field *E* indicated.

In PEEM we direct an ultrafast linearly polarized laser beam onto a groove milled into the ITO substrate by FIB. At the groove light scatters into the ITO via diffraction and is guided for a short distance until it interacts with a gold platelet located on the surface as shown in Fig. 1. In a way similar to the SPR prism coupling method of Kretschmann [34], favorable alignment of wave propagation constants permits energy transfer of the photonic mode to a SPP mode. The dielectric constant of the ITO increases the momentum of light to the point where coupling to a SPP on the metal's surface is possible via tunneling. Due to factors such as the lossy character of the metal and its thinness [35], the resonance line width is broadened and there is a narrow spread to the wave numbers that satisfy momentum conservation. The highest coupling efficiency occurs where the mismatch δ vanishes in

$$k_x = k_{SPP} + \delta, \tag{1}$$

where k_x is the horizontal component of the wavenumber of the guided light in the ITO and k_{SPP} is the real part of the complex SPP propagation constant β [36].

#200567 - $15.00 USD Received 4 Nov 2013; revised 26 Nov 2013; accepted 27 Nov 2013; published 4 Dec 2013

The SPP-enhanced photoemission yield observed in PEEM can be switched on and off by switching the incident laser from p- to s-polarization (TM to TE). PEEM images capture the entire wave propagation from groove to platelet as a series of interference fringes produced between the incident laser and guided modes. Image analysis centers on the interference fringes, from which we obtain the in-plane wave speeds of the modes and compare them to analytic solutions. We look for a favorable match between photonic and SPP modes.

While the modes of a planar photonic waveguide are readily obtained from waveguide theory, the theoretical determination of SPP modes is complicated for thin metals. Ordinarily a metal/dielectric interface can support a single TM-polarized SPP mode. When the metal is thin the modes of the interfaces in close proximity become coupled and their propagation constants deviate from isolated mode solutions [37]. The coupled bound 'supermodes' that arise are the symmetric field mode (s_b) and asymmetric field mode (a_b). The symmetry refers to the transverse fields (H_y and E_z) across the interfaces. Important for the problem of waveguide to SPP mode coupling is the energy distribution (given by the Poynting vector as shown in Fig. 2). The energy of the s_b mode tends to be less confined and favors the vacuum layer. As a result its momentum is more like that of a free vacuum mode than a waveguide mode. In contrast the energy of the a_b mode is concentrated in the ITO. It is therefore the a_b mode whose momentum has the best chance to match that of a waveguide mode.

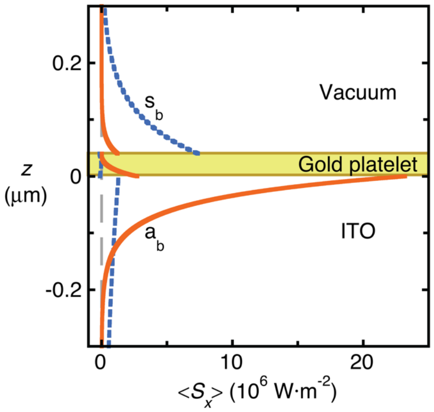

Fig. 2. Time-averaged Poynting vector $\langle S_x \rangle$ of the asymmetric field (a_b) and symmetric field (s_b) SPP modes of a 3-layer slab model comprised of ITO, a 40-nm thick gold platelet, and vacuum. Scale normalized such that each SPP wave carries 1 watt per meter along the y-axis, with the x-axis being the propagation direction.

Analytic models for the two SPP modes of three-layer systems were developed in the 80's and 90's [38–40] and can now readily be solved by modern desktop computers. The advantage of using analytic models, rather than commercially available software, is a deeper understanding of the compatibility between photonic modes of waveguides and of SPP modes of metal films. To illustrate this advantage we present the waveguide and SPP mode solutions graphically. In evaluating the solutions for the waveguide and SPP modes, we show that energy transfer from the waveguide to the a_b SPP is possible due to a coincidence of wavenumbers (or the equivalent effective indices). We shall see that the effective index $n_{eff}(a_b) = k_{SPP}/k_0 = k_{SPP} \cdot c/\omega$ of the a_b mode varies strongly with gold thickness. An experimental consequence is strong selectivity for gold platelets for thickness such that $n_{eff}(a_b) \sim n_{eff}(\text{waveguide})$.

2. Experiment

The gold platelet in the study was selected from a deposition of platelets prepared by reduction of chloroauric acid in aniline. The aniline restricts growth on the $\{111\}$ plane and leads to the production of thin atomically flat single crystals [41]. The gold platelets were drop-deposited onto a 15 Ω/□, 275 ± 15-nm thick [Fig. 3(a)] ITO-coated 0.2-mm borosilicate glass coverslip (SPI Supplies, Inc.). The platelets have a wide distribution of shapes, which include hexagons, triangles, rods, and quantum dots. The trapezoidal platelet used in the study was selected in part for its thinness, which was $d = 35 \pm 5$ nm as best determined from tilted-view SEM [Fig. 3(b)]. By chance there were two gold quantum dots on top of the platelet, which proved to be interesting as they generated localized SPPs. To create an input port to the photonic waveguide we used a dual-beam focused ion beam (FEI Co.) to mill a 100-nm wide groove perpendicular to the light beam approximately two microns from the gold platelet. To minimize contamination of the specimen only the milled area of the groove was exposed to the gallium beam. Additionally, the region was prepared for milling and imaged using the FIB's electron beam, which was used at low current and for the shortest possible time.

The specimen was illuminated by one of two lasers incident at $\theta = 60°$ to the surface normal: a 15-mW frequency-doubled CW argon ion laser ($\lambda_0 = 244$ nm) and a 150-mW frequency-doubled Ti:sapphire laser ($\lambda_0 = 410$ nm; FWHM = 5 nm) with pulse width ~80 fs and repetition rate of 80 MHz. The laser spot size at the sample was about 50×100 μm^2. Polarization was set with a tunable wave plate. Our homebuilt PEEM is aberration-corrected with an electrostatic mirror [42,43]. In best conditions and at high magnification lateral resolution of the instrument is 5 nm, but in this experiment the pixel size limit to resolution is 30 nm in UV and 60 nm in blue. Image exposure times were 30 sec for UV incident light, 6 min for blue p-polarized light (TM), or 14 min for blue s-polarized light (TE).

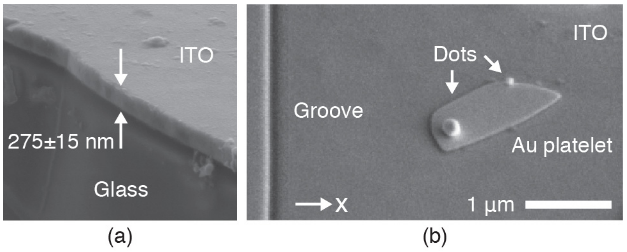

Fig. 3. SEM of the substrate and specimen. (a) edge of ITO/glass substrate viewed at 70° from surface normal. (b) gold platelet and two gold quantum dots on ITO substrate near the FIB-milled groove viewed at 55° from the surface normal.

The photonic modes in the ITO as well as the SPP modes in the gold platelet generate an interference pattern with the light of the incident laser. The interference pattern constitutes a stationary intensity variation and results in a modulated photoemission (PE) yield. For the duration of the exposure, the PE yield Y is the time average of the electric field raised to $2n$ power, where n is the number of photons needed for the photo-excitation of a single electron [16,19,44]. For the laser light field E_0 and the guided or diffracted field E_r, the PE yield from the two-dimensional plane (x,y), or equivalently (r, ϕ), is given as

$$Y(r) = \int_0^{t_0} \left| E_0(r,t) + E_r(r,t) \right|^{2n} dt. \tag{2}$$

The field $E_r(r,t)$ can be of photonic or plasmonic origin. If the two fields are plane waves, the functions have the form

$$\begin{aligned} E_0(r,t) &= E_0 \exp\left[i\left(k_0 r \sin\theta \cos\phi - \omega t \right) \right]; \\ E_r(r,t) &= E_r \exp\left[-r/2L \right] \exp\left[i\left(k_r r - \omega t + \zeta \right) \right], \end{aligned} \tag{3}$$

where the wavenumber of light in vacuum is $k_0 = \omega/c$ and the wavenumber of the guided or diffracted wave is k_r. For a guided photonic mode, $k_r = n_{eff} k_0$, where n_{eff} is the effective index

#200567 - $15.00 USD Received 4 Nov 2013; revised 26 Nov 2013; accepted 27 Nov 2013; published 4 Dec 2013

of the waveguide. For a SPP, $k_r = k_{SPP} = \mathrm{Re}[\beta]$, which we can solve for using electromagnetic theory and optical constants. The angle of incidence of the laser light in the (x,z) plane is θ. The angle ϕ is the direction of the guided mode relative to the light vector projected on the (x,y) surface plane. The angle ζ accounts for a possible phase shift. The important $1/e$ propagation length of the guided wave is L.

Carrying out the integration in Eq. (2) one finds that the PE yield has a spatially constant background contribution given by $(E_0^{2n} + E_r^{2n})$, and a spatial modulation whose frequency depends on the difference of the propagation constants and relative directions of the waves. Typically the incident laser field is large compared to that of the second wave ($E_0 >> E_r$). The modulation contrast is then dominated by the term containing $E_0^{2n-1}E_r$ and higher order terms containing E_r can be neglected. As a result the observed modulation of the PE yield is in leading order, proportional to the electric field of the diffracted or guided wave.

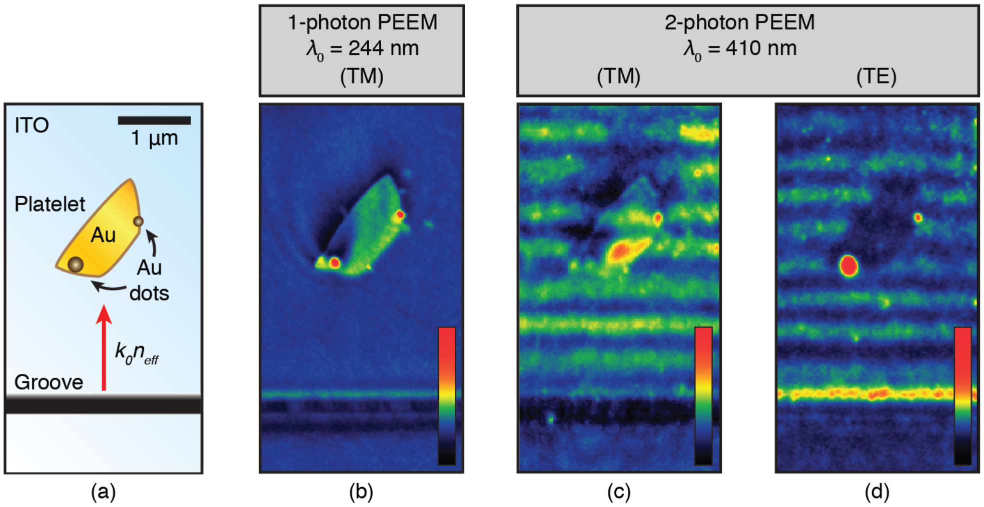

Fig. 4. False-color PEEM micrographs of a gold platelet on an ITO thin film waveguide. Color scales indicate relative PE yield. (a) Identification key for objects seen in the images. Direction of guided light, which enters via the groove indicated. (b) 1-photon PEEM for reference. (c) 2-photon PEEM with excitation light TM-polarized. Light guided by the film appears as interference fringes. Photoelectron emission from the gold flake is enhanced by SPPs produced by energy transfer from the waveguide. (d) 2-photon PEEM with the excitation light TE-polarized. Since the guided TE-polarized light cannot generate SPPs, photoelectron emission from the platelet is low. The gold quantum dots are bright due to localized SPP enhancement.

3. Results

Single-photon UV 1P-PEEM and two photon 2P-PEEM images of the specimen are arranged for comparison in Fig. 4. In the UV, ITO is opaque. The specimen appears in a similar way as it would in SEM [Fig. 4(b)]. We see the ITO substrate, FIB-milled groove in the ITO, and gold platelet and particles with mostly topographical detail plus some yield modulation due to diffraction. In 2P-PEEM the images are very different [Fig. 4(c) and Fig. 4(d)]. The most obvious difference is a series of horizontal bands due to interference between the incident laser and the guided photonic modes. To emphasize these bands we present the images in false-color. The bands appear in both TM and TE polarization, although with differences in spacing and phase due to differences in the waveguide modes of each polarization [45].

Our focus is the marked difference in the appearance of the gold platelet when illuminated by TM- versus TE-polarized blue light. When the incident laser is TM-polarized the gold platelet has bright bands across it that appears similar to the fringes on ITO but with a small lag in phase [Fig. 4(c)]. Fringes do not appear on the platelet when the laser is TE-polarized [Fig. 4(d)]. Furthermore, beyond the platelet the fringes on ITO are sharply diminished in TM polarization while they appear unperturbed in TE polarization [Fig. 5]. These findings are consistent with the coupling of a photonic mode in ITO to a SPP mode in the gold platelet. Sharply diminished fringes following the platelet suggest that energy lost to a SPP occurs with some degree of efficiency.

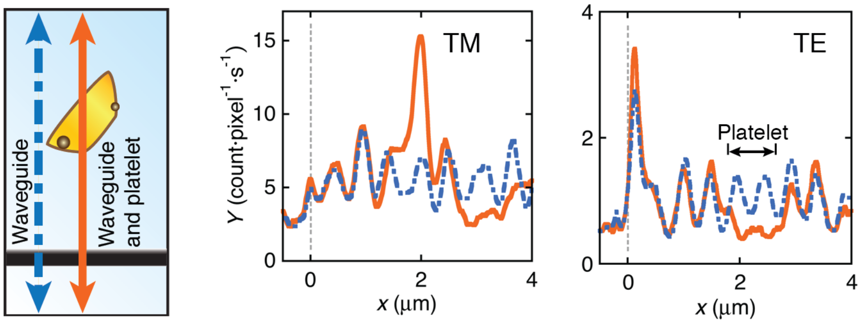

(a) (b) (c)

Fig. 5. Comparison of photoemission yields along recorded along lines across the ITO waveguide alone (dashed) and across the ITO waveguide and gold platelet (solid) as indicated in (a). (b) When the laser has TM polarization the platelet exhibits strong PE. Beyond the platelet PE yield is low. (c) When the laser has TE polarization PE yield from the platelet is very low. Beyond the platelet the yield is similar to the basic ITO waveguide. A pixel represents 20 × 20 nm^2.

On close inspection of Fig. 4(c), we notice some enhanced photoemission at the border of the platelet. This can be caused by the photonic edge diffraction as well as by SPPs excited in the complex near-fields that exist in diffraction. In cases reported elsewhere for gold, silver, and silicon [19,24] edge-related 2-photon photoemission can be great—possibly many times the baseline PE level. The relatively low edge brightness of this platelet might be due to its thinness (d~$\lambda/10$) or a lack of edge sharpness. In our case, edge effects are small compared to the interference fringes.

We note that the gold quantum dots appear very bright in TE polarization. The appearance of brightness is partly relative since PE yield is generally low in the TE case (for ITO, Y_{TM}/Y_{TE} ~5). Nonetheless PE yields from the gold nanoparticles are comparable between the two polarizations. For the smaller nanoparticle Y_{TM}/Y_{TE} is about 3. Conversely, for the large nanoparticle Y_{TM}/Y_{TE} is about 0.5. These observations are qualitatively consistent with theories for localized SP resonance of metal spheres on a metal surface [46]. As small spheres the nanoparticles can be thought of as small dipole antennas paired with induced image charges inside the metal substrate. A dipole and its image interact differently to the two types of polarizations, with the TE case being most like that of a free particle [47,48].

4. Discussion

The quality of the PEEM images allows a high level of analysis [17]. We can use the geometry of the experiment, wavelength of the laser, and spacing of interference fringes on ITO to obtain the velocities of the photonic modes. The propagation constants of the photonic modes in ITO, $k_x = k_0 n_{eff}$, can be calculated accurately from waveguide theory [45]. Similarly, we can calculate the propagation constants of the SPP modes on the gold platelet with the three-layer slab models of Burke [38] and others [39,40].

4.1. Photonic waveguide modes

To understand how the interference fringes develop consider two wavefronts of the laser incident at angle θ. Referring to Fig. 6(a), the leading wavefront of the laser (w = 0) generates a surface wave at point O. The surface wave radiates in all directions in the (x,y) plane with velocity $v = c/n_{eff}$. The distance D between constructive interference fringes can be found using the criteria of equal time of flight for the surface wave traveling the path $\overline{\mathrm{OQ}}$ and the light wave on path $\overline{\mathrm{PQ}}$:

$$D = \frac{\lambda_0}{c/v - \sin\theta\cos\phi}. \tag{4}$$

In the case of the guided wave in ITO, the groove is a line source perpendicular to the plane of incidence. When $\phi = 0$ we may simplify Eq. (4) and recast it terms of n_{eff} as

$$n_{eff} = \frac{\lambda_0}{D} + \sin\theta. \tag{5}$$

The task is then to determine D from the images and find n_{eff} using Eq. (5).

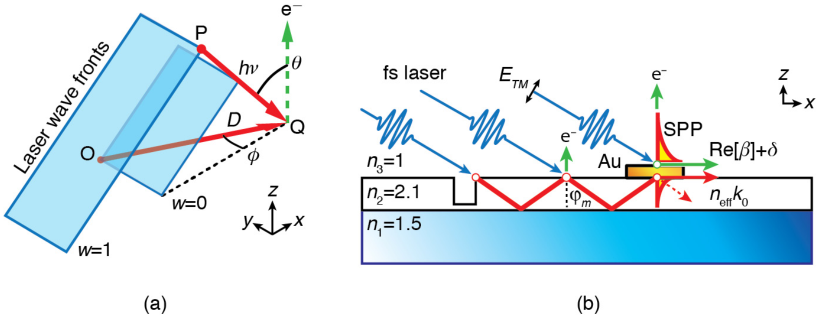

Fig. 6. Optical model for interference between a surface wave and incident laser. (a) the first laser wavefront generates a surface wave at point O. A second wavefront overtakes the surface wave at point Q leading to interference in the photoemission yield. (b) ray-model of a waveguide and of the generation of a SPP in a manner similar to the Kretschmann prism method. The guided TM wave generates a SPP on gold when the waveguide effective index is approximately equal to the SPP propagation constant relative to light, i.e. $n_{eff} \sim \mathrm{Re}[\beta]/k_0$.

The ITO film permits two overlapping photonic modes for each polarization. To disentangle these two modes, we apply a discrete Fourier transform (the FFT are plotted in Fig. 7) and find strong spatial periods of D = 476 ± 13 nm for TE and D = 528 ± 22 nm for TM. Using Eq. (5) we find for the effective index in ITO: n_{eff} = 1.73 ± 0.03 for TE and 1.64 ± 0.03 for TM. We will show below that these are the m = 1 modes of the waveguide. We also find a lesser m = 0 mode in each case with n_{eff} = 2.02 ± 0.07 for TE and 1.94 ± 0.05 for TM.

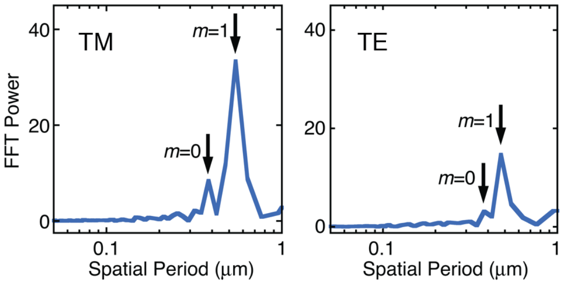

Fig. 7. FFT periodograms of ITO waveguide yield profiles taken along dashed lines indicated in Fig. 5(a) for x>0. The two peaks correspond to the m = 0 and m = 1 waveguide modes. The profiles were processed with the Welch window function.

We can use the amplitudes of the peaks in the FFT power spectrum to estimate the relative strengths of the two photonic modes. This will be important when we later consider the photonic to plasmonic coupling efficiencies. Remembering that the modulation in the PE yield is proportional to the fields of the guided modes [Eq. (2)], the ratio of the waveguide coupling efficiencies $n_m = (E_r / E_0)^2$ is approximately the ratio of the squared amplitudes found in the FFTs. For both the TE and TM cases, the yields of $m = 1$ modes are about 4-5 times those of $m = 0$ modes. The ratio of the coupling efficiencies of the modes is therefore about twenty, i.e. $\eta_{m=1}/\eta_{m=0}$ ~20.

If the thickness d of the ITO film can be measured independently, the effective indices may be calculated from waveguide theory. We measured a cross sectional ITO thickness of $d = 275 \pm 15$ nm [Fig. 3(a)]. For a thin slab the solutions to the waveguide satisfy, for TM polarization [45],

$$k_0 n_2 d \cos\varphi_m - m\pi = \tan^{-1}\left[n_2 \frac{\sqrt{n_2^2 \sin^2\varphi_m - n_1^2}}{n_1^2 \cos\varphi_m}\right] + \tan^{-1}\left[n_2 \frac{\sqrt{n_2^2 \sin^2\varphi_m - n_3^2}}{n_3^2 \cos\varphi_m}\right] \quad (6)$$

and for TE polarization,

$$k_0 n_2 d \cos\varphi_m - m\pi = \tan^{-1}\left[\frac{\sqrt{\sin^2\varphi_m - (n_1/n_2)^2}}{\cos\varphi_m}\right] + \tan^{-1}\left[\frac{\sqrt{\sin^2\varphi_m - (n_3/n_2)^2}}{\cos\varphi_m}\right]. \quad (7)$$

The refractive indices n_1, n_2, and n_3 correspond to the layers of glass, ITO, and vacuum, respectively. The angle φ_μ is the internal angle of reflection for mode m as indicated in Fig. 6(b), from which $n_{eff}(m) = n_2 \sin\varphi_m$. The terms on the right-hand side are the Goos-Hänchen phase shifts needed to satisfy the internal ray path distance and phase matching boundary conditions. As an analogue to the forthcoming method used to solve for SPP modes, we solve Eqs. (6) and (7) graphically as shown in Fig. 8(a). We find good agreement with the FFT results for the $m = 1$ modes equal to $n_{eff} = 1.77 \pm 0.03$ for TE and 1.67 ± 0.04 for TM. The lesser $m = 0$ modes, $n_{eff} = 2.01 \pm 0.01$ for TE and 1.99 ± 0.01 for TM, are consistent as well. The corresponding internal angles for the $m = 1$ modes are $\varphi_1 = 58°$ and 53°, for TE and TM respectively. Interestingly, these angles are not very different from the incident angle. Evidently the complicated edge diffraction at the groove's edge favors the mode with the smallest deflection angle [49]. We can explore hypothetical ITO waveguides by solving Eq. (6) over a range of film thicknesses as we have done in Fig. 8(b). From this plot we see that the effective indices of the available ITO modes are strongly dependent on film thickness.

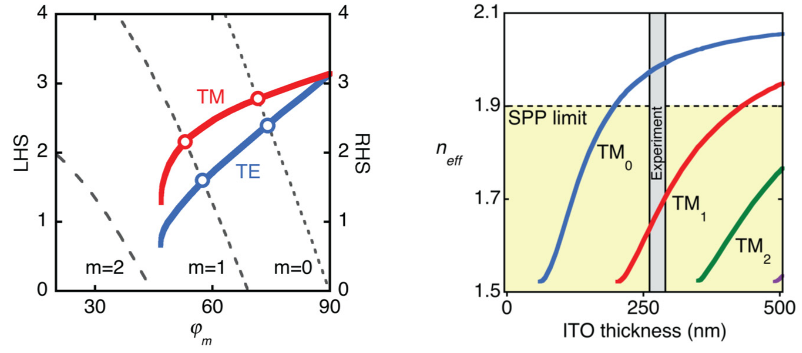

(a) (b)

Fig. 8. Vacuum/ITO/glass slab waveguide solutions. (a) Geometrical method of solution of Eqs. (6) and (7) for modes of an ITO film of thickness 275 nm. LHS in dashed lines and RHS in solid lines. (b) Effective indices of TM waveguide modes as a function ITO thickness. The film used in the study indicated by the vertical bar. The upper limit for SPPs [from Fig. 10(b)] suggests that the TM$_0$ mode of the present ITO waveguide is not available for plasmonic coupling.

4.2. Surface plasmon polariton modes

We now turn to the SPPs. A simplistic approach is to use the well-known [50] single-interface solution for a SPP where its complex propagation constant β is

$$\beta = k_0 \sqrt{\frac{\epsilon_1 \epsilon_2}{\epsilon_1 + \epsilon_2}}. \tag{8}$$

The dielectric constant of the insulating layer is ϵ_1 and complex dielectric constant of the metal is ϵ_2. The SPP wavenumber k_{SPP} and its characteristic propagation length L_{SPP} follow from β

$$\begin{aligned} k_{SPP} &= \mathrm{Re}[\beta]; \\ L_{SPP} &= \left(2\,\mathrm{Im}[\beta]\right)^{-1}. \end{aligned} \tag{9}$$

In the present case, we can profit by a more advanced treatment. Because the gold is very thin (d = 35 ± 5 nm), the non-leaky bound SPP modes of each side of the metal superimpose to form the coupled symmetric (s_b) and asymmetric (a_b) 'supermodes' mentioned above. From a practical stand point, these two supermodes differ in three important ways: range, confinement, and momentum. Near a certain limiting cutoff thickness the s_b solution can have a range much greater than the bulk mode (tens of microns or more). For this reason the s_b mode is often called the long-range mode. The s_b mode generally has low spatial confinement with fields that extend far into the boundary dielectric layers [Fig. 2]. As a result the s_b mode has high velocity and hence low n_{eff}, which makes for a poor match to waveguide modes. In contrast, the a_b mode is more spatially confined, not limited by thickness, shorter ranged, and more importantly, has generally high n_{eff}, which is more suitable to waveguide coupling. In our configuration, the wavenumbers of the two modes deviate from the single-mode solutions of the simple vacuum/gold and gold/ITO interfaces for gold thicknesses less than ~80 nm.

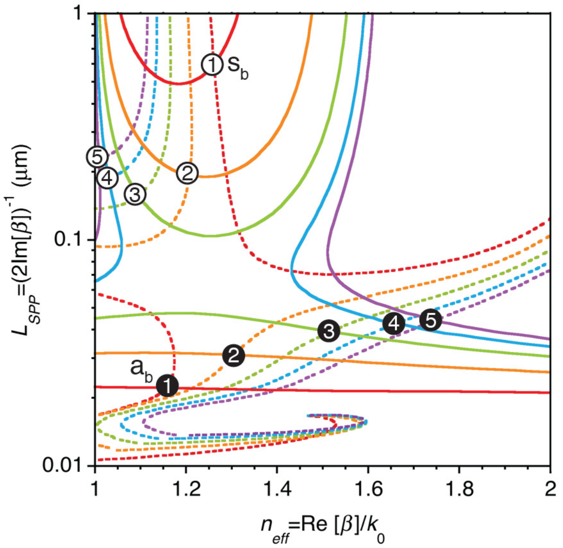

Fig. 9. Graphical method of solution of Eq. (10) for the SPP supermodes of a three-layer slab model of vacuum/gold/ITO. In complex space we plot the propagation constants β that independently satisfy the real and imaginary parts of Eq. (10), which are shown as solid and dashed lines, respectively. Complete solutions exist where real and imaginary lines intersect. There are generally two solutions for each gold thickness d, which correspond to the s_b and a_b modes. Solutions for five gold film thicknesses shown: (1) 25 nm, (2) 30 nm, (3) 35 nm, (4), 40 nm, and (5) 45 nm.

#200567 - $15.00 USD Received 4 Nov 2013; revised 26 Nov 2013; accepted 27 Nov 2013; published 4 Dec 2013

To calculate the propagation constants of the supermodes we first make the simplification of ignoring the finite horizontal dimensions of the platelet, which would contribute additional fine structure to the solutions [51]. Continuity of the tangential components of the electric fields at the interfaces demands that the complex propagation constants β satisfy [38,40]

$$\exp\left(-2\alpha_2 d\right)+\frac{\left(\epsilon_1\alpha_2+\epsilon_2\alpha_1\right)\left(\epsilon_2\alpha_3+\epsilon_3\alpha_2\right)}{\left(\epsilon_1\alpha_2-\epsilon_2\alpha_1\right)\left(\epsilon_2\alpha_3-\epsilon_3\alpha_2\right)}=0, \tag{10}$$

where the coefficients α_s for each layer s are

$$\alpha_s=\sqrt{\beta^2-\epsilon_s k_0^2}. \tag{11}$$

This formalism assumes that for the two dielectric layers $\epsilon_1 \geq \epsilon_3$. Solution of Eq. (10) can be accomplished numerically or graphically by solving for the real and imaginary parts separately [Fig. 9]. Except for very thin films, where d<cutoff thickness and the s_b mode disappears, β has two physically meaningful solutions corresponding to the s_b and a_b modes.

For comparison with experiment we consider the asymmetric three-layer model of gold (ϵ_2) sandwiched between ITO (ϵ_1) and vacuum (ϵ_3). ITO is a comparatively poor conductor with a surface plasmon resonance in the infrared region at 0.8 eV [52]. At optical frequencies we can treat it as a pure dielectric with $\epsilon_1 = 4.4$ at $\lambda_0 = 410$ nm [53]. For gold we use Johnson and Christy's optical data [54]. At $\lambda_0 = 410$ nm, $\epsilon_2 = -1.69 + 5.72i$.

In Fig. 10 we plot the propagation constants obtained from Eq. (10) together with the photonic modes obtained previously. We find that the effective index of the SPP, $\mathrm{Re}[\beta]/k_0$, strongly varies in the region of the gold platelet's thickness (30 nm ≤ d ≤ 40 nm). Most importantly we find an intersection between the a_b mode and $m = 1$ photonic mode at d~40 nm ($k_x = k_{spp} = 1.7k_0$). Here the coupling mismatch δ would be zero and photonic to SPP mode conversion would be the most efficient. The momentum match for the s_b mode is never very close to either photonic mode. We also note that this region contains the minimum of the s_b mode's propagation distance and throughout the range $L_{SPP} < 200$ nm [Fig. 10(b)]. This is considerably less than the propagation length calculated in a simple two-layer model, i.e., $L_{SPP} = 380$ nm. The propagation distance of the a_b mode is shorter still at L_{SPP} ~40 nm.

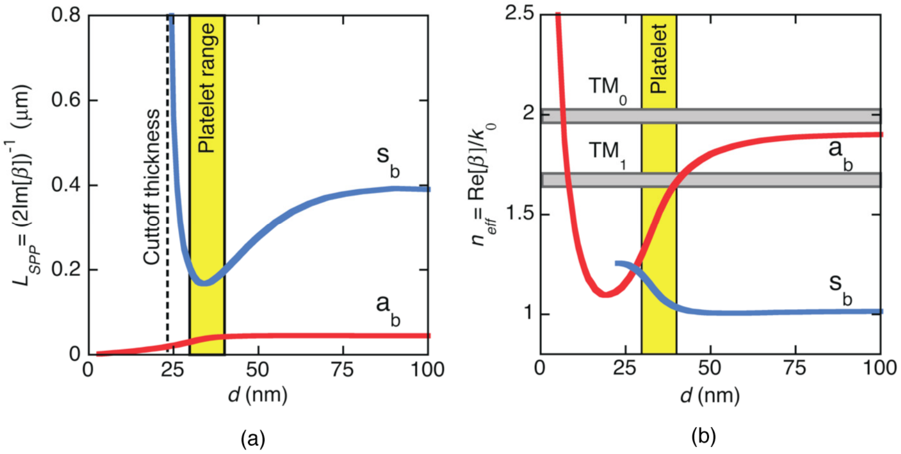

Fig. 10. SPP supermodes for gold thickness d calculated from the three-layer slab model of vacuum/gold/ITO at $\lambda_0 = 410$ nm. (a) propagation distance of the SPP supermodes. (b) effective index of the symmetric s_b and asymmetric a_b modes plotted with the TM photonic modes of the ITO waveguide. The vertical bar indicates the estimated thickness range of the gold platelet. The waveguide TM_1 mode coincides with the a_b mode at d ~40 nm.

#200567 - $15.00 USD Received 4 Nov 2013; revised 26 Nov 2013; accepted 27 Nov 2013; published 4 Dec 2013

For efficient transfer of energy between modes, the difference δ between propagation constants k_x and k_{SPP} should be small [Eq. (1)]. In the SPR prism analogue, coupling efficiency falls dramatically when δ is more than a percent or two of k_{SPP} [35]. Referring to the PEEM image and intensity profiles [Figs. 4 and 5], we note two important features. The observed PE yield enhancement due to the SPP is significant. Therefore δ is small. But we also observe significant PE enhancement across the 1-μm platelet, which is much longer than the mode propagation lengths. Therefore energy transfer is not optimal, meaning δ is probably small but nonzero. With these points in mind, we can rule out the weak $m = 0$ photonic mode, for even in the best case, $\delta \sim 0.3k_0$. We can also rule out the s_b mode, for which $\delta > 0.5k_0$. By this process of elimination, we conclude that energy transfer occurs between the $m = 1$ TM mode and a_b SPP mode and that the gold platelet is nearly 40 nm thick.

If we return to Fig. 8(b), we see that we need to carefully consider both the thickness of the gold and the ITO in order to ensure that a suitable ITO mode is available for coupling to a SPP mode. In the present case, only the ITO TM_1 mode can couple to a SPP mode, and the SPP mode must be the a_b mode. For this combination, however, the matching is excellent.

We must still explain why we see enhanced PE across the 1-μm length of the platelet. A coupling efficiency of just 2-3% per 40 nm of distance (equal to L_{SPP}) is sufficient to reduce a photonic mode by more than 90% over 1 μm as observed. This in turn results in near total conversion of photonic to SPP energy over the length of the gold platelet (1 μm). Thus the SPP modes are continually fed from below as highly damped driven oscillations.

We can speculate what the PE might look like in a case of very high conversion efficiency. The photonic mode would be consumed in a short distance by the a_b mode, which rapidly decays since $L_{SPP} = 40$ nm. Accordingly, the leading edge of the platelet would appear very bright. Without the underlying photonic mode, the gold's surface would be dim save for very widely spaced fringes caused by interference between the incident laser and other fields. Namely diffracted light or the s_b mode excited by the near fields of edge diffraction [24]. As in the image shown here, with all TM photonic energy transferred to a SPP there will be no interference fringes beyond the platelet, which is in contrast to the TE case.

5. Conclusion

We have shown in PEEM the direct observation of bound photonic modes in an ITO waveguide and the conversion of one photonic mode to a SPP mode on a thin gold platelet. The photonic modes guided by the ITO thin film are well described by infinite slab waveguide theory. SPP mode calculation is more complicated since the single-crystalline gold platelets produced by the chemical growth method are thin. The three-layer slab model predicts the existence of two bound SPP modes—the symmetric field mode s_b and asymmetric field mode a_b. To conserve momentum, photonic to SPP conversion occurs with highest likelihood between the TM_1 mode of the waveguide and the a_b SPP mode of the gold platelet. Because the propagation distance of the a_b mode is short and SPP-enhanced emission is visible across the 1–μm platelet, we can conclude that the coupling efficiency between these two waves is low. We estimate a conversion efficiency of a few percent per a_b propagation length of L_{SPP} ~40 nm. This is sufficient to reduce the photonic mode by more than 90% within 1 μm.

From this example we also conclude that energy transfer to SPP will probably be limited to the a_b mode since n_{eff} of the s_b mode is near unity. Experiments on s_b mode coupling will continue to need other methods that satisfy momentum conservation, e.g., edge diffraction coupling, end-fire coupling, or grating coupling [37]. For practical applications it may appear that the short range a_b mode is less useful than the long range s_b mode, particularly for plasmonic waveguides. Nonetheless, the a_b mode finds applications where high spatial confinement is required [55–57]. If needed, the range of the a_b mode can be extended to several microns by use of red or near-IR excitation light. This spectral region is well within the range of two-photon PEEM when known techniques for altering work functions are applied, as for example, cesium coatings [58]. The example presented here shows that a detailed experimental analysis of dynamic energy transfer in photonic/plasmonic hybrid systems can be obtained. The results are a further demonstration of PEEM's promise as an experimental tool in this research area and for the development of integrated planar photonics.

Acknowledgment

This work was supported by the US-DOE Basic Science Office contract DE-FG02-13ER46406.